Journal of Power Sources 196 (2011) 8773–8788

Contents lists available at ScienceDirect

Journal of Power Sources

journal homepage: www.elsevier.com/locate/jpowsour

Carbon honeycomb grids for advanced lead-acid batteries. Part I: Proof of concept☆

Angel Kirchev*, Nina Kircheva, Marion Perrin

Laboratoire de Stockage de l'Electricté, Institut National de l'Energie Solaire, Commissariat à l'Energie Atomique et Energies Alternatives (CEA), 50 Avenue du Lac Léman – Lynx 3, BP332, 73377 Le Bourget du Lac, France

ARTICLE INFO

Article history:
Received 4 April 2011
Received in revised form 18 May 2011
Accepted 3 June 2011
Available online 12 June 2011

Keywords:
Carbon honeycomb grid
Lead acid battery
AGM
VRLAB
Positive plate impedance
Grid corrosion

ABSTRACT

The carbon honeycomb grid is proposed as innovative solution for high energy density lead acid battery. The proof of concept is demonstrated, developing grids suitable for the small capacity, scale of valve-regulated lead acid batteries with 2.5–3 Ah plates. The manufacturing of the grids, includes fast, known and simple processes which can be rescaled for mass production with a minimum, investment costs. The most critical process of green composite carbonisation by heating in inert, atmosphere from 200 to 1000 °C takes about 5 h, guaranteeing the low cost of the grids. An AGM–VRLA, cell with prototype positive plate based on the lead–2% tin electroplated carbon honeycomb grid and, conventional negative plates is cycled demonstrating 191 deep cycles. The impedance spectroscopy, measurements indicate the grid performance remains acceptable despite the evolution of the corrosion, processes during the cycling.

1. Introduction

In the past decade the huge variations in the oil prices along with the increasing demands for reduction of the CO_2 emissions renewed the interest in the electric "zero emission" transport. Due to its low cost, high safety and efficient recycling infrastructure, the valve-regulated lead-acid batteries (VRLAB) remained relatively strong market competitor of the concurrent nickel and lithium-ion based storage systems in applications like electric bicycles, scooters and small electric cars especially in countries with low average incomes. However, regarding the forthcoming electric vehicle (EV) and plug-in hybrid electric vehicle (PHEV) markets, the lead-acid battery was "thrown" out the competition due to its low energy density. The huge difference between the theoretical energy density of 168 Wh kg^{-1} and the typical values of about 35 Wh kg^{-1} are mainly due to the inefficient use of the lead and its components, which comprises about 67% of the total battery weight [1]. The grids of the positive and negative plates are the heaviest components serving only to support mechanically the active materials and to collect the electric current generated by the charge/discharge process. They comprise between 33 and 50% of the plate weight (active material to grid ratio varies from 1:1 to 2:1 depending on the particular technology). The utilisation of the active materials is also relatively low—typically between 40 and 50% of the lead or the lead dioxide can be converted to lead sulphate during a 10 h-rated discharge. As a result, 65–75% of the lead does not participate in the electrochemical reactions of energy storage and generation. Hence the improvement of the lead-acid battery energy density is still an open challenge.

In the past two decades several research teams proposed different types of carbon or carbon foams as a promising alternative to the classical cast or punched grids:

- Peterson and Ahlberg suggested that the monolithic glass-like carbon can serve as grid material without giving practical demonstration of the concept [2].
- Czerwiński and Żelazowska proposed Reticulated Vitreous Carbon (RVC®, glass-like carbon foam) as grid material in [3,4]. Further RVC® was used to develop grids by Gyegne et al. [5,6]. Recently, Czerwiński et al. compared the performance of bare RVC electrodes and Pb-electroplated ones, both types pasted with negative active material (NAM) [7,8]. The results of this comparison indicated that conductivity of the bare RVC is good enough to support charge/discharge currents in the range of C_n/1 h (where C_n is the electrode or cell nominal capacity in [Ah]).
- Kelley and co-workers proposed carbon foam lead-acid battery grid technology described in a series of patents applied by the start-up company Firefly Energy (presently Firefly International Energy) [9–12]. Despite that the company announced in 2008 the

☆ This work has been reported during the 12th European Lead Battery Conference.

* Corresponding author. Tel.: +33 4 79 44 45 49; fax: +33 4 79 68 80 49.
E-mail address: angel.kirchev@cea.fr (A. Kirchev).

0378-7753/$ – see front matter © 2011 Elsevier B.V. All rights reserved.
doi:10.1016/j.jpowsour.2011.06.021

launch of their OASIS™ battery up to the moment no data about the performance of this technology can be found in the literature.
- Chen et al. published a series of papers on the development of small positive and negative pasted electrodes using pitch-based carbon foam [13–17].
- Jang et al. studied graphite foam electrodes pasted with positive active material (PAM) and negative active material (NAM) [18] indicating that the graphite foam material [19] has much better electric and thermal conductivity.

The main advantage of the foam-type current collectors is the large surface area making possible to decrease the so-called "γ" coefficient representing the ratio of the active material weight per unit of current collector surface area [20]. Since the hydrogen overvoltage on the above-mentioned carbon materials is relatively high and the process of hydrogen evolution does not have destructive impact on the carbon structure, the carbon foams of different types can be used without modifications as grid materials. However the direct use of carbon as a positive grid material is hardly possible up to now. The main reason is a destructive corrosion-like process of the carbon surface flaking caused by the process of oxygen evolution which proceeds in similar way and gives similar final result in acid, neutral and alkaline electrolytes [18,21–23]. Similar effect is observed when glass-like carbon surface is treated with Fenton solution, i.e. when the surface is chemically attacked by OH• radicals [24]. As a result of this, if bare carbon structure (foam, spine, etc.) is pasted with basic lead sulphate paste, the process of oxygen evolution on the carbon surface runs in parallel with the positive plate formation and charge processes resulting in progressive detachment of the active material from the carbon current collector [18]. The usual strategy to employ the carbon foam as a positive grid material is to electroplate it with lead or lead–tin coating [5,6]. In this way, the pasted electrodes can withstand prolonged cycling because the lead metal coating resembles very well the surface of the classical lead-acid battery grids and works as a protective layer over the carbon.

2. Carbon honeycomb grid concept

Despite the excellent surface to volume ratio, which is the main advantage of the foam as a lead-acid battery grid material, there are several problems between the "foam grid concept" and the practical realisation of grids which can be employed in the existing schemes of lead-acid battery assembly. From one hand it is the pasting process where the paste should be forced into the foam pores—it supposes the combined use of foams with bigger cell-size and pastes with lower density/consistency resulting probably in poor performance in terms of cycle life and energy density. Because of the reticulated 3D structure of the foams, the pasting can be mechanically "difficult" and the foam could be crushed during this process. From the other hand at large-scale battery plates, foam grid alone cannot collect efficiently the current generated during the cycling. The solution of adding a massive frame and top-lug of lead bonded to the perimeter of the foam slab as proposed by Gyenge et al. [6] can be enough efficient. However combined with the electroplated lead, the grid weight becomes too high.

In attempt to propose an alternative of the carbon foam, the carbon honeycomb grid technology was developed at the Laboratory for Storage of the Electricity of the French Commission for Atomic and Alternative Energies (LSE—CEA) [25].

The composite honeycomb structures are well-known materials used in different constructions requiring very high strength to weight ratios [26]. When the composite honeycomb structure is constituted of suitable materials, for example cellulose-based paper impregnated with thermosetting resin [27] or pitch [28], it can be subjected to carbonisation by heating in inert atmosphere up to 1000–3000 °C. The resulting carbon/carbon composite structures retain the inherited honeycomb geometry obtaining some new properties, the most important of which is the electric conductivity.

The honeycombs alone are hardly useful as grids in the same manner as it was discussed above in the case of carbon foams. That's why the manufacturing scheme presented in Fig. 1 was developed. The first stage consists in the choice of suitable "green" composite honeycomb core with the desired dimensions. In the second stage a frame of thermosetting composite material is moulded along the honeycomb core keeping the honeycomb channels empty. Note that this process is compatible only with honeycomb core structures due to the unique parallel arrangement of the channels typical for these structures. After the hardening of the frame, the resulting block is cut to slices with a desired thickness during the third stage—these will be the "green" honeycomb grids. After the heat treatment procedures applied during stage 4, the resulting all-carbon/carbon composite grids consist of carbon honeycomb core connected to a massive carbon frame having a top-lug, resembling well the typical lead-acid battery grid. The frame ensures the mechanical stability of the grid and the efficient colleting of the electric current. The top-lug allows using the cast-on-strap process where the plates from the same polarity are connected in parallel within the lead-acid cell. The last manufacturing stage is the surface treatment of the carbon honeycomb grids. Here the main process is the lead electroplating. It may be preceded by chemical or electrochemical etching in order to improve the adhesion of the lead coating, however this step is optional.

The honeycomb grids offer several strategic advantages. The first one is the increase of the active materials utilisation. From one hand the decrease of the plate thickness enhances the sulphuric acid transport from the AGM separator (in the case of VRLA batteries) to the core of the plate, especially at high current discharge rates [29]. From the other hand the decrease of the grid mesh dimension (in the case of honeycomb grids this parameter is the half of the honeycomb cell size [26]) increases the active mass utilisation. This effect is first discussed in details by Faber in [30]. According to the data published by Faber, honeycomb grids with cell size in the range of 2–3 mm (grid mesh dimension 1–1.5 mm) should deliver 60–65% positive active mass utilisation or 135–145 Ah kg^{-1}. For cell size in the range of 1 mm the PAM utilisation is even 80%. The second advantage is the high γ-coefficient, due to the good surface to volume ratio of the honeycomb structures. The third advantage is the efficient use of the compression in the case of AGM–VRLAB technology. Fig. 2 illustrates a fragment of the active block assembly where the two AGM separator sheets exert a compression on both side of the honeycomb channel. It can be supposed "a priori" that even low levels of compression will maintain a good contact between the active material and the internal walls of the honeycomb channel. The same cannot be said for the carbon foam grids due to their reticulated 3D structure—in this case the compression will be "absorbed" rather by the foam instead of the active materials.

The aim of this work is to present the proof of carbon honeycomb grid concept demonstrating its capabilities as the positive plate current collectors.

3. Experimental

3.1. Honeycomb core and honeycomb block

The honeycomb core used in this work was prepared using the easiest available material for this purpose—a corrugated paperboard with two layers scavenged from waste packaging. The

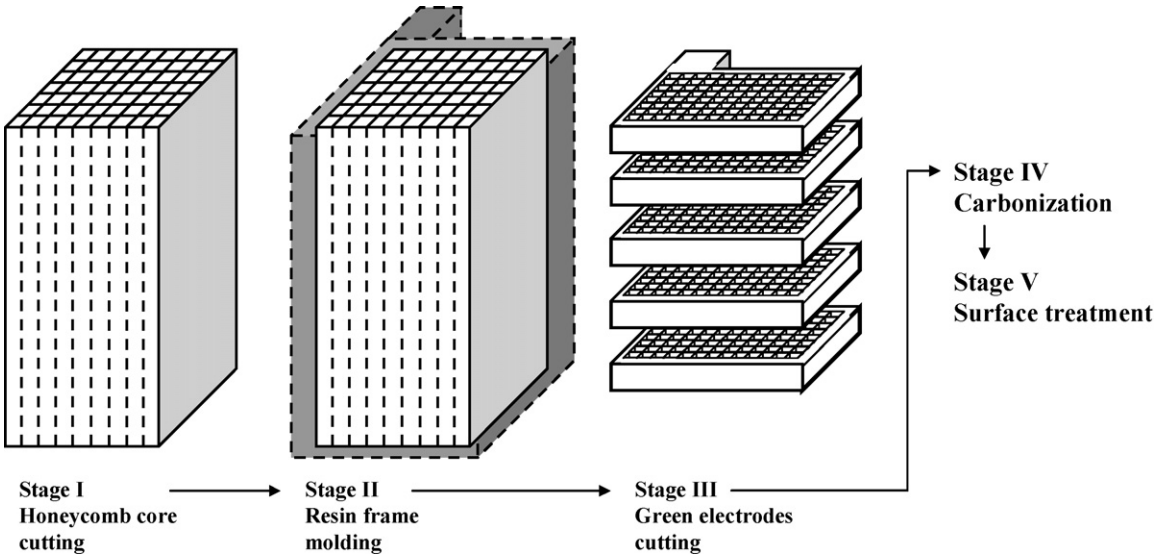

Fig. 1. Manufacturing scheme of the carbon honeycomb grid production.

paperboard thickness was 7 mm with internal distance between the parallel sheets ~4 and ~3 mm for the first and the second layer, respectively. These two distances will correspond to the two sizes of the honeycomb block cells. The ashes content of the paperboard was 8%, a value typical for this class of materials. This value was obtained following the international standard ISO 2144 [31]—the material is dried at 105 °C for 16 h, weighted and fired at 900 °C in air for 2 h.

The paperboard was cut to plates of 75 mm width and 170 mm length. Nine paperboard plates were stacked together using for glue a mixture of liquid phenol-formaldehyde resin (resole) CELLOBOND® J2027L and curing agent (catalyst) CELLOBOND® Phencat 382 in ratio 100 weight parts of resin and 5 weight parts of catalyst. Both the resin and the catalyst were provided by Hexion Specialty Chemicals, Inc., Louisville, KY, USA (presently Momentive Specialty Chemicals Inc.). The block was left for 5 h at 60 °C for curing of the liquid phenol-formaldehyde resin and so bonding the paperboard sheets together. The impregnation of the block with liquid phenol-formaldehyde resin was performed in two times by multiple pouring of CELLOBOND® J2027L, CELLOBOND® Phencat 382 and ethanol mixture in proportion of 100:5:20 (weight parts) through the honeycomb channels followed by the same curing procedure as mentioned above. Here the ethanol was used to reduce the resin viscosity and to facilitate the impregnation. After the impregnation, the bottom ends of the channels were blocked and few layers of cotton gauze were wrapped around the honeycomb block and placed in specially designed mould. The mould was filled with a mixture of CELLOBOND® J2027L, CELLOBOND® Phencat 382 and ethanol in proportion 100:5:20 (weight parts) and left for curing at 50 °C for 24 h. After the curing the mould was dismounted and the resulting honeycomb block was sliced to "green" honeycomb grids with thickness between 3.5 and 4.5 mm using general purpose band-saw. Good precision of the cutting was not possible to achieve due to the type of the tool, however the green composite happened to be very robust and easy for cutting. Fig. 3 presents the end fragment of the moulded honeycomb block after the cutting of about 25 grids.

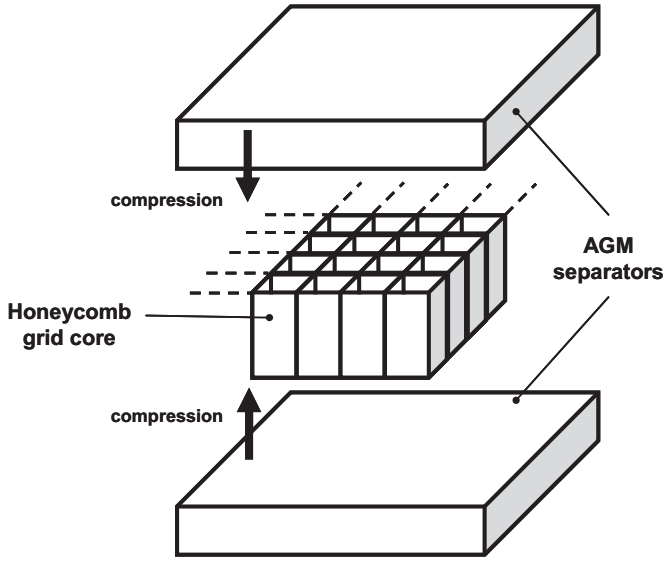

Fig. 2. Scheme of the cell assembly using AGM separators and plates with honeycomb grids.

Fig. 3. End fragment of the moulded honeycomb block after the cutting of about 25 grids.

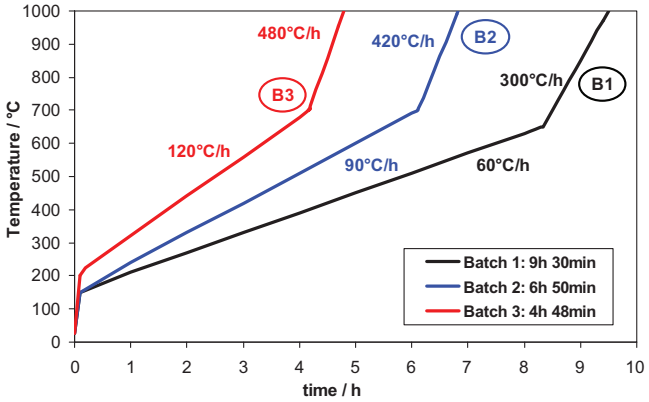

Fig. 4. Heat treating programs of carbonisation of three batches of carbon honeycomb grids.

3.2. Carbonisation of the honeycomb grids

The heat treatment of the grids was carried out in two separate stages. In the first stage, which can be denoted as "drying", the grids were heated in air atmosphere from 25 to 195 °C with a rate of 12 °C h^{-1} and left at 195 °C for 6 h. During this process the ethanol and the water escape the solid matrix of the resin leaving some open porous structure. The main contribution to the creation of the open porous structure is due to the ethanol which is volatile enough. Further the open porous structure greatly accelerates the second heat treatment stage which will be denoted as "carbonisation" [32]. The carbonisation of the honeycomb grids consists in heating from 200 to 1000 °C in nitrogen atmosphere. During this process the polymers are converted into carbon and small gaseous molecules like water, carbon dioxide, carbon monoxide, methane and hydrogen [33]. The open porosity created during the drying stage allows easy evacuation of these gases without the creation of substantial pressure gradients inside the polymer matrix which may cause fracture of the composite [32].

Three batches of six grids were carbonised with the three temperature profiles plotted in Fig. 4. The temperature profile consists of slower heating from 200 to 650–700 °C and faster heating from 650–700 to 1000 °C. The first stage is slower because it corresponds to much more intensive evolution of gaseous products and composite shrinkage. During the second stage only small portions of hydrogen escape the composite matrix and the evolution of the shrinkage with the temperature is much less severe [34].

All the resulting grids from the three series were without apparent defects and with good mechanical strength. Fragments cut from the grids before and after the carbonisation were embedded in epoxy resin moulds, polished and characterized using light optical microscopy.

The shrinkage during the carbonisation was about 21–22%, and the carbon yield was about 55–60% (vs. the weight after the drying at 195 °C).

3.3. Electric conductivity and density of the carbon grids

In order to evaluate the conductivity of the carbon/carbon composite of the frame and the honeycomb core, two different samples were prepared for electrical resistance measurements in the following way:

- A rectangular prismatic section of the frame running in parallel with the corrugated sheets with length of 4.6 cm and with and thickens of 0.3 cm was cut from the grid. Both ends were electroplated with 5 μm copper (1 M $CuSO_4$ and 0.5 M H_2SO_4 plating bath, plating current density 30 mA cm^{-2}) covering two 0.5 cm sections of the sample's length. A pair of cables were soldered to the copper-coated sections in order to get four-point type of connection required for the adequate resistance measurements.
- A nearly prismatic section of the honeycomb core of the grid corresponding to two plain parallel sheets of the paperboard bonded together during the honeycomb core fabrication with length of 4.3 cm, width of 0.4 cm and thickness of 0.6 mm was cut from the grid and the sticking parts of the corrugated honeycomb walls were removed mechanically. Both ends of the sample were coated with copper in the above-mentioned way leaving 3.3 cm of the sample length with bare carbon. Again two pairs of cables were soldered allowing the use of four-point type of connection scheme.

The electrical resistance of the samples was measured using potentiostat/galvanostat SOLARTRON Multistat 1470 connected with frequency response analyzer SOLARTRON FRA 1250 using DC and AC methods. In the DC method, the current trough the sample was swept linearly from 0 to 4 A with 100 mA s^{-1} and the resistance was calculated from the slope of the voltage vs. current plot. In the AC method, the ohmic resistance of the samples was obtained from the impedance spectra point where the imaginary component is zero—the EIS plots were "purely" inductive, corresponding to a resistor in series with an inductor. Both types of samples showed practically the same specific resistance value equal to 0.014 Ω cm or 71 S cm^{-1} in terms of specific conductivity. Same values were obtained from the DC and the AC methods.

Approximate estimation of the apparent density of the carbonized honeycomb core and the frame was done using a volumetric flask of 50 cm^3 as a pycnometer and de-ionized water as a reference liquid with density of 0.998 g cm^{-3} at 22 °C. The value obtained for the frame of the grid was 1.09 g cm^{-3}. The apparent density of the honeycomb core was 1.24 g cm^{-3}.

For the sake of comparison, the specific resistance and density of the monolithic non-porous commercial-grade glass-like carbon are correspondingly 0.005 Ω cm and 1.54 g cm^{-3} [35], while for the porous bulky monolithic glass-like carbon prepared by Rautavuori and Törmälä these values are 0.026 Ω cm and 1.20 g cm^{-3} [32].

3.4. Electroplating of the carbon honeycomb grids

The electroplating of the carbon honeycomb grids was done using p-phenolsulphonic bath with the following composition: lead p-phenolsulphonate 200 g dm^{-3}, tin p-phenolsulphonate 6.35 g dm^{-3}, free phenolsulphonic acid 40 g dm^{-3}, gelatine 0.5 g cm^{-3} and low molecular weight sodium lignosulphonate (average M_w 8000, average M_n 3000, ALDRICH) 0.5 g dm^{-3}. The weight ratio between the lead and the tin (as metals) in the electrolyte is 98:2 in order to achieve a coating with approximate composition Pb–2%Sn. Part of the sodium lignosulphonate precipitated and was removed by filtration. The anodes were made of lead wire with diameter of 2 mm, which was corrugated to resemble flat plate using lead–tin welding spots as tin sources distributed evenly on the lead anode surface. The acid p-phenolsulphonic baths were employed in the Soviet industry for lead, tin and lead–tin (solder) plating, delivering brighter coatings with better adhesion to the substrate in comparison with the more typical fluoroborate and fluorosilicate acid electrolytes [36–40].

The geometrical surface of the carbon honeycomb grid was calculated approximating the cross-section profile of the honeycomb cells to triangular (with two sizes of triangles corresponding to the two corrugated sheets), resulting in area of 180 cm^2. Before the plating the carbon grid was washed with ethanol in ultrasound bath for 5 min, and dried for 2 h at 60 °C. The electroplating was

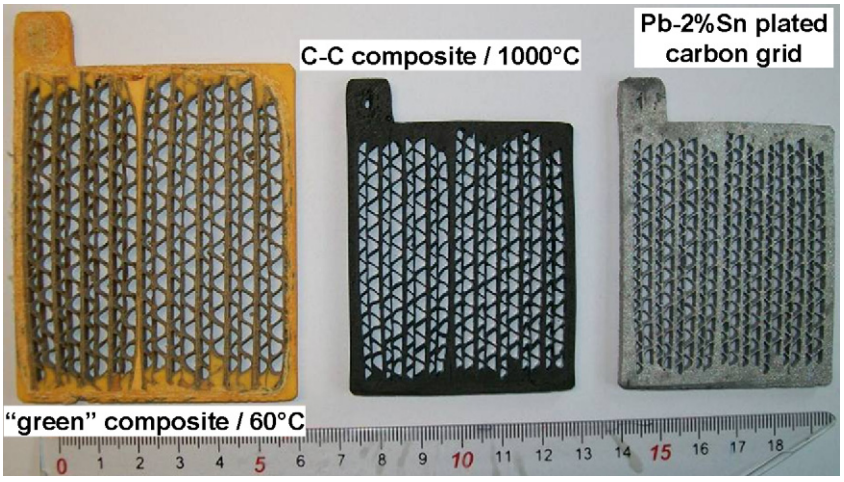

Fig. 5. Evolution of the carbon honeycomb grid after the sawing, the carbonisation and the lead–tin electroplating (the ruler below is in centimetres).

done with a current of 1.6 A for 3 h and 20 min. At these conditions the thickness of the lead–tin coating should be about 100 μm at 100% faradic efficiency of the electrodeposition process. A set of three grids, one on the left after the slicing of the honeycomb block, a second after the carbonisation and the last on the right after the electroplating are shown in Fig. 5.

3.5. Prototype VRLA cell with carbon-based positive grid

One honeycomb grid with a thickness ~4 mm was pasted with basic lead sulphate paste prepared in the following way: 50 g of battery-grade leady oxide (STECO Power, FRANCE) with 20% unoxidized Pb content was hand-mixed first with 5 g of deionised water. Than 9.9 g of H_2SO_4 solution with specific gravity of 1.40 g cm^{-3} was added in a drop-by-drop manner during the mixing. Finally, one more gram of water was added and the paste was mixed two more minutes, giving a total time of paste preparation of about 15 min. The paste was inserted in the honeycomb cells of the grid using wooden spatula. The pasted plate together with the unused paste was left to cure at room temperature (22 °C) for 72 h and were dried for 24 h at 60 °C. A sample of the dried and cured paste was analyzed chemically. The quantity of unoxidized lead was less than 1%, the concentration of the lead oxide was 69.5% and the concentration of the lead sulphate was considered to be equal to 30.5%.

The weight of each component of the prototype plate is as follows:

- carbon honeycomb grid: 7.489 g,
- Pb–2%Sn coating (100 μm): 18.691 g (total grid weight: 26.180 g),
- dried paste: 25.626 g.

Considering that the honeycomb surface in contact with the paste is about 170 cm^2, the value of the gamma coefficient representing the PAM weight to grid surface area ratio is $\gamma \sim 0.15$ g cm^{-2}.

Using the data from the chemical analysis it was calculated that the total Ah-equivalent of the paste is 5.66 Ah. Considering a reference utilisation of PAM equal to 50%, the nominal capacity of the plate was chosen to be 2.83 Ah. The charge and discharge rates were calculated using this value of the nominal capacity.

Prior to the formation process, a 2 mm thick lead wire was passed trough a specially drilled hole in the centre of the top-lug (Fig. 5), and the zone between the wire and the lug was welded using lead–tin solder. The welding zone was further protected by a layer of epoxy resin and thermo-shrinkable gauntlet.

The formation of the plate was carried out in sulphuric acid electrolyte with initial specific gravity of 1.125 g cm^{-3} after 2 h of soaking. Two cured negative plates re-cut from corresponding SLI cured plates (STECO Power, France) were used as counter electrodes. During the formation 11.32 Ah were injected in a multi-step algorithm for a period of 36 h. After the formation the prototype positive plate was washed and dried at 60 °C for 16 h.

A VRLA cell was assembled using the dry-charged prototype positive plate, two dry-charged negative plates with a thickness of 3.5 mm re-cut from industrial negative plate (CEAC-EXIDE, FRANCE) and 440 g m^{-2} AGM separator enveloping both sides of the negative plates. The applied compression of ~20% was achieved using plastic plates as spacers. ABS cell casings were provided by First National Battery. The carbon honeycomb grid size was specially developed to fit in this type of VRLAB box using previously obtained data about the composite shrinkage during the carbonisation. The cell was sealed using custom-made lid and epoxy resin. A silver/silver sulphate reference electrode with 1.28 g cm^{-3} specific gravity electrolyte [41,42] was fit in the cell using epoxy-based paste for sealing. The atmosphere in the cell was regulated by a vent-plug scavenged from used VRLAB using an epoxy-sealed polypropylene connector and PVC tube. Pictures of the cell before and after the sealing of the lid and fitting of the reference electrode and the vent are presented in Fig. 6. The cell was filled with H_2SO_4 electrolyte with specific gravity of 1.24 g cm^{-3} until the appearance of "water mirror" above the edge of the AGM separator. The complete saturation of the active block (the positive plate, the negative plates and AGM separator) was achieved placing the cell in a vacuum chamber thus evacuating most of the air trapped in the smaller pores. The quantity of the filled electrolyte was 53 g or 42.7 cm^3, corresponding to an electrochemical equivalent of 4.795 Ah. This equivalent will be used in the calculations of the coefficient of sulphuric acid utilisation as an active material.

The formation and the subsequent cycling of the prototype VRLA cell was performed using potentiostat/galvanostat SOLARTRON Multistat 1470 connected with frequency response analyzer SOLARTRON FRA 1250 for impedance spectroscopy measurements. The impedance spectra were recorded in the frequency range 65 kHz–10 mHz, in potentiostatic mode at the open circuit potential of the positive plate, applying AC amplitude of 5 mV. The positive plate was connected as working electrode during all measurements, and the cell voltage was monitored simultaneously using an auxiliary voltage channel. The use of auxiliary voltage channel allowed also measuring simultaneously the total cell impedance in the moment of positive plate impedance spectroscopy measurement. The negative plate impedance was deduced from the total cell impedance.

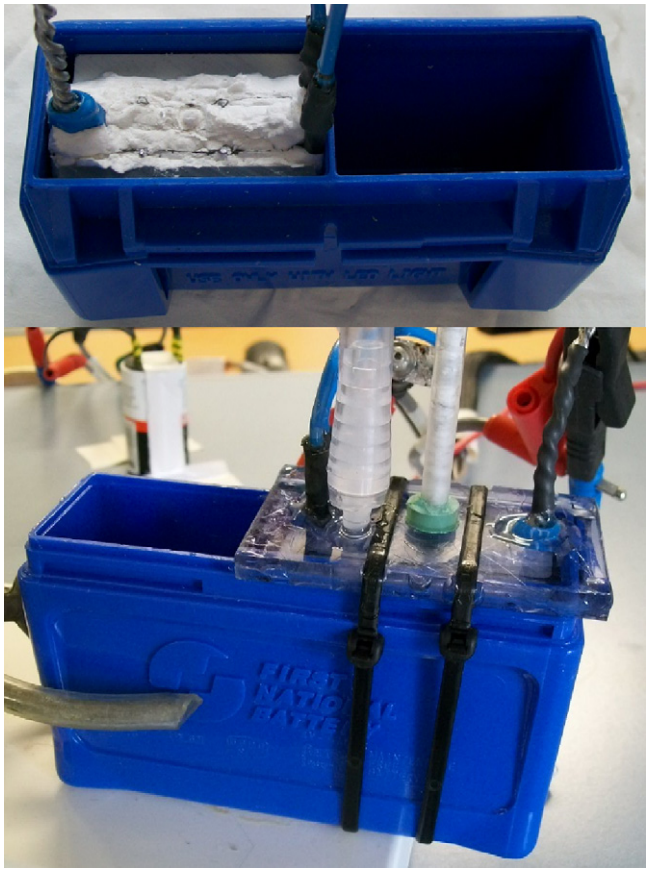

Fig. 6. Photographs of the VRLA cell after the assembly of the active block (up) and during the operation after the sealing of the lid (down).

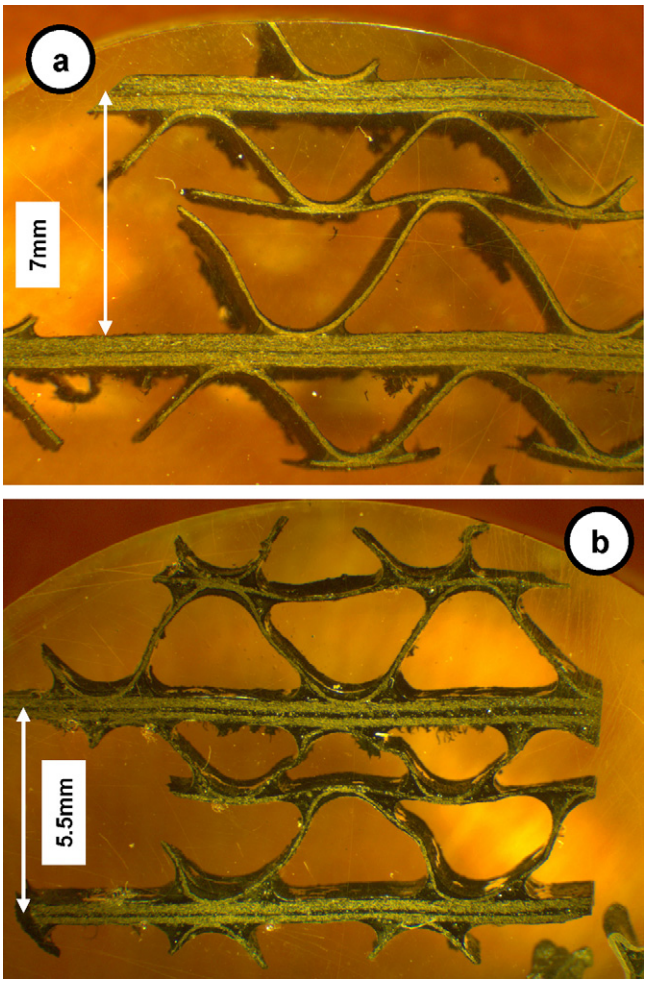

Fig. 7. Stereo microscope images of "dried" (a) and carbonised (b) honeycomb cores.

4. Results and discussion

4.1. Microstructure of the carbon honeycomb grid

Considering its microstructure, the carbon honeycomb grid consists of three principal "zones"—a frame surrounding the honeycomb core, a honeycomb core and a zone of contact between them. All three zones retain the microstructure of the corresponding "green" composite during the carbonisation process due to the absence of melting processes (regarding the carbon derived both by the phenolic resin and the cellulose) between 200 and 1000 °C. A comparison between "dried" and carbonised honeycomb cores is presented in Fig. 7. The stereo microscope images show that the honeycomb core shrinks about 21–22% however the structure is preserved almost perfectly. It should be noted that the honeycomb wall deformations which can be observed in Fig. 7b correspond to original deformations in the corrugated paper, i.e. they are not a result from the shrinkage. A comparison between the honeycomb microstructure before and after the carbonisation in the zone of two plain parallel sheets of the honeycomb core is presented in Fig. 8a (green composite) and b (carbon/carbon composite). It can be seen that the layered structure of the paper/resin composite is retained almost perfectly during the pyrolysis process.

The zone of the contact between the honeycomb core and the frame of the grid in the part where the frame runs in parallel with the so-called "ribbon" direction (the direction parallel with the plane of the corrugated paper sheets) is presented in Fig. 9 (the sample was cut from a grid, electroplated and embedded in epoxy resin). The difference between the honeycomb core and the frame is recognizable even with the low magnification of the stereo microscope image (Fig. 9a). It can be seen that the contact between the top sheet and the frame is good and continuous. The patterns of the cotton fibres used to reinforce the green composite can be distinguished too. Fig. 9b shows a closer view of the above-mentioned contact zone obtained by light optical microscopy. Four types of structures can be distinguished easy. On the left of Fig. 9b, there is the typical view of carbonised honeycomb core in the zone of the node point between plain and corrugated sheet. The patterns of the carbonised cellulose fibres are embedded into a glass-like carbon matrix with low porosity. On the right of Fig. 9b it can be seen the microstructure of the frame consisting of microporous glass-like matrix containing macropores corresponding to the location of the cotton fibres. A zoom-view of the interface between the frame and the honeycomb core is presented in Fig. 9c. It can be seen that the only difference between the glass-like carbon matrix of the honeycomb core and the frame is in their porosity. The absence of pores in the carbon honeycomb part is due to nearly complete evaporation of the ethanol (and water) during the hardening process after the impregnation. Such very early evaporation of the ethanol is not possible to occur in the frame, where the initial resin cross-linking (i.e. hardening) proceeding is the mould. The ethanol is removed after the cutting and the drying of the grids leaving a system of open micropores with relatively narrow pore size distribution.

4.2. Microstructure of the copper/lead–tin and lead–tin coating

The glass-like carbon and its composites cannot be wetted by most liquid metals and alloys, especially the ones with low melting points like the lead. That's why the top lug of the grid in the zone

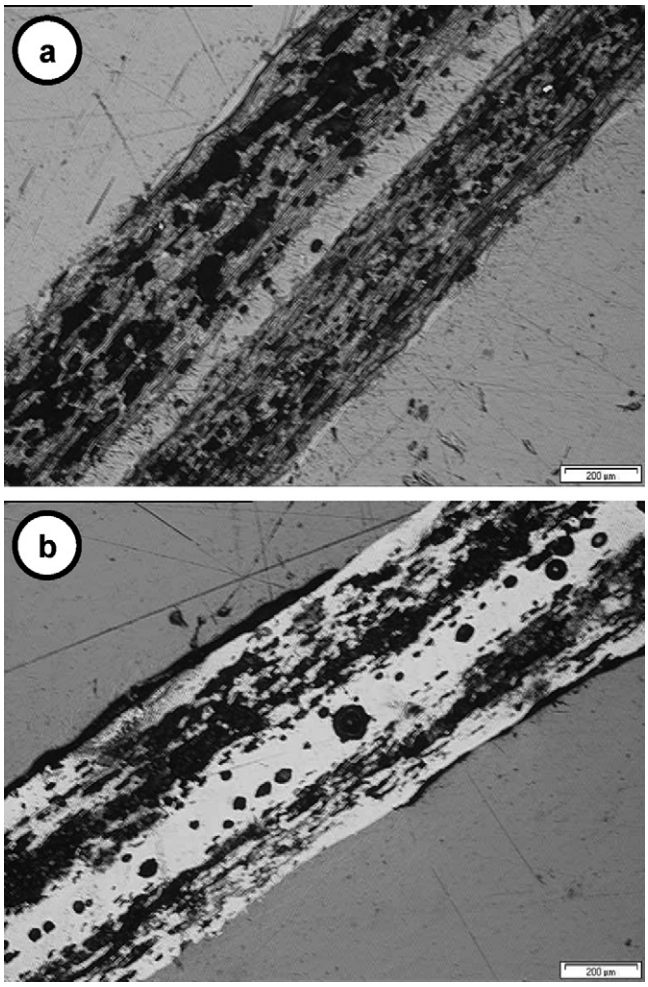

Fig. 8. Optical micrographs of "dried" (a) and carbonised (b) honeycomb cores in the zone where two plain-parallel sheets of corrugated paperboard are bond together.

of the cast-on-strap connection should be coated with a thin layer of metal with high melting point and low solubility in liquid lead. This requirement is necessary because the liquid lead mould of the cast-on-strap may strip the lead–tin coating resulting in bad contact between the plate and top lead. The copper coating is the best option to avoid such a phenomenon in terms of cost, strength of the contact with lead and lead-alloys and simplicity of the process. The porous structure of the frame contributed greatly to the adhesion strength of the copper coating. The adhesion was tested qualitatively by scratching with scalpel and metal brush– the instruments leaves shiny patters in the same way as the scratching of massive copper samples. The carbon substrate becomes visible only after continuous scratching. Similar results were observed for the adhesion strength of the lead–tin alloy both on the bare carbon and copper-coated carbon composite.

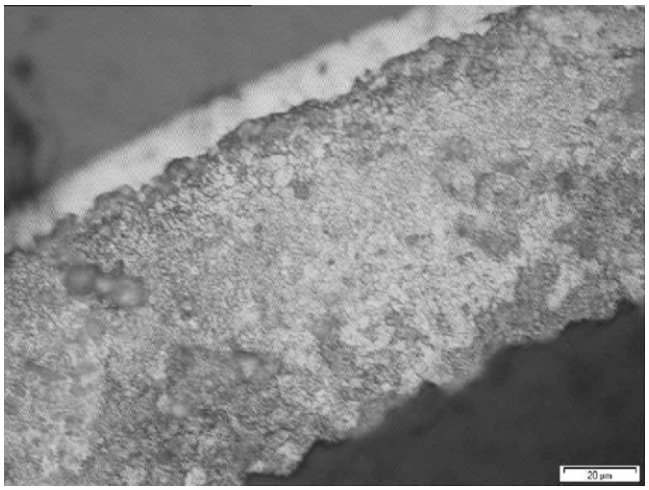

Fig. 10. Optical micrograph of etched coating (copper and lead–tin) of electroplated grid frame fragment—the focus of the microscope in on the thicker lead–tin layer.

The sample shown in Fig. 9a bears combined copper (10 μm)/lead–tin (100 μm) coating. The coating thickness is homogeneous and bright. The surface of the sample was treated with etching solution of 7 weight parts of glycerol, 2 parts of concentrated nitric acid and 1 part of glacial acetic acid for 20 s at 40 °C [43]. An optical micrograph of the etched lead–tin coating is shown in Fig. 10. The coating microstructure is cellular with grain size in the order of several microns. The copper sub-layer appears as a very bright pattern which is out of focus due to different etching rate.

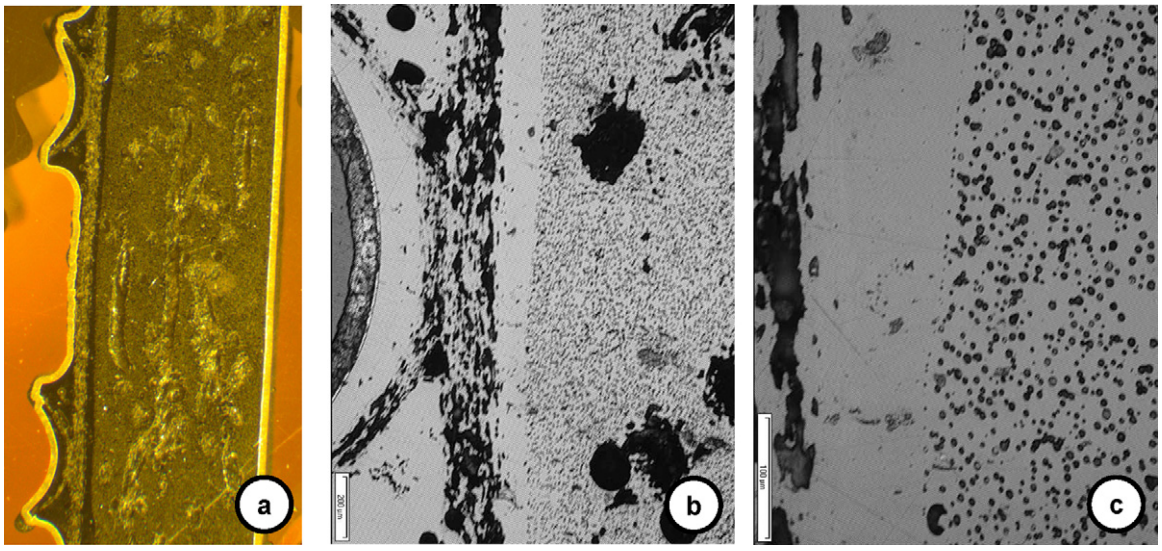

Fig. 9. Stereo microscope image (a) and optical micrographs (b and c) of copper and lead–tin electroplated grid fragment in the zone between the carbon honeycomb core and the massive carbon frame.

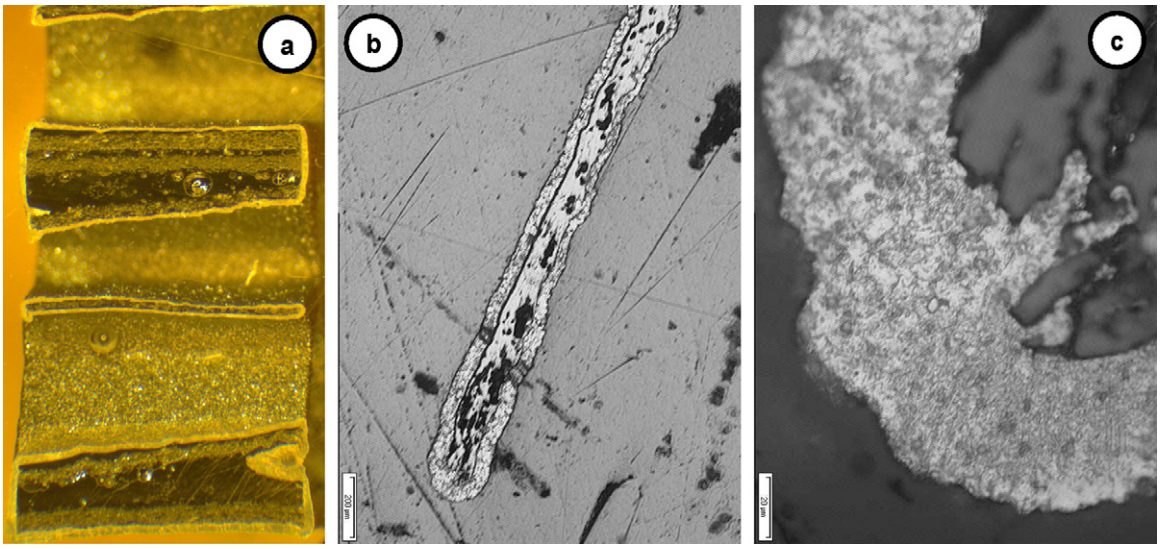

Fig. 11. Stereo microscope image (a) and optical micrographs (b and c) of carbon honeycomb core fragment with electroplated lead–tin coating—the cross-section is perpendicular to the plane of the grid.

Another lead–tin electroplated carbon honeycomb sample showing the distribution of the coating thickness along the length of the honeycomb channels walls is shown in Fig. 11a (stereo microscope image). A closer view of the thin channel wall cross-section is given in Fig. 11b indicating relatively homogeneous and adherent lead–tin coating. Fig. 11c presents high magnification micrograph of the etched lead–tin coating in the zone of the edge of the honeycomb cell wall (i.e. at the surface of the grid). It can be seen that the surface defects of the carbon honeycomb composite are filled with metal in depth of several tens of micrometers. The microstructure of the alloy revealed by the etching is very similar to the one shown in Fig. 10.

4.3. Initial cycling of the VRLA cell with carbon honeycomb grid positive plate

The evolution of the positive (a) and the negative (b) half-cell potentials, the cell voltage and the current during the first three cycles are plotted in Fig. 12. During the initial five cycles the cell is discharged with 20 h-rated current or $C_n/20$ h, where C_n is the nominal capacity equal to 2.83 Ah corresponding to 50% utilisation of the positive active material. The recharge was performed with a current $C_n/3$ h up to positive plate potential equal to 1.3 V vs. the reference electrode ($Ag/Ag_2SO_4/5\ M\ H_2SO_4$) and further applying this potential for 5 h. The initial discharge capacity is quite low (the utilisation of PAM in the first cycle is only 26%), however it increases rapidly with the cycling. This result is due to an incomplete formation (many white spots remained on the plate after the formation) from one hand, and high thickness of the plate from the other. The negative plate potential remains almost constant during the discharge due to the huge excess of negative active material. In the beginning of the charge, right after the first cycle, one can observe the appearance of the voltage spike associated with the development of corrosion layer with increased resistance typical for positive plates with antimony-free grids [44,45]. The positive plate potential transient during the recharge resembles well the results published by Pavlov [44,45], obtained for cycling of small-sized pasted positive electrodes cycled in classical three-electrode cell configuration using $Hg/Hg_2SO_4/H_2SO_4$ reference electrode. Fig. 12c shows that in the end of the third cycle the negative half-cell reaches completely charged state—it is due to the fact that the original dry-charged negative plates were in stock for about 7 years.

The impedance spectra measured in the end of the charge for the first three cycles are shown in Fig. 13. The impedance of the positive plate (Fig. 13a) and the total cell impedance (Fig. 13c) were measured simultaneously using one auxiliary voltage channel, while the negative half-cell impedance was calculated from the difference. The validity of this approach was confirmed in separate measurements. The results from Fig. 13 show that the ohmic resistance of the cell and the positive plate increase substantially between the first and second cycle, while the ohmic resistance of the negative plates remains practically constant. Considering the appearance of the positive plate potential peak in the beginning of the charge (Fig. 12a and c) in the same time, it can be supposed that this initial increase of the internal resistance of the positive plate (and the cell internal resistance too) is due to the development of the so-called Active Mass Collecting Layer (AMCL) which acts as an interface between the PAM and the corrosion layer [20]. The comparison between the ohmic resistance of the positive plate and both negative plates at the end of the first cycle (i.e. prior to the formation of the thick corrosion layer) shows that the lead–tin electroplated carbon honeycomb grid could be a promising current collector for high-rate applications. The comparison between the low-frequency impedance of the positive plate and both negative plates is also interesting—in the end of the third cycle the low frequency impedance of both negative plates is markedly higher than those of the positive plate regardless of the substantial oversizing of the negative half-cell, which is typical for the conventional pasted positive plates.

4.4. Performance of the prototype positive plate at the maximum of its capacity

During the cycle life testing, the VRLA cell was discharged with a current $C_n/5$ h down to a cut-off positive plate potential of 0.75 V vs. the reference electrode and recharged in constant current/constant potential (CCCP) mode starting with current $C_n/1$ h and limiting the positive plate potential at 1.3 V. Prior to the CCCP charge mode a constant current of $C_n/1$ h was applied without any limit for 10 min due to the appearance of the above-mentioned voltage spike in the beginning of the charge. The duration of the constant potential stage of the charge was adjusted several times in order to deliver values of the charge factor (F_{ch}, the percentage ratio between the recharged Amp-hours and the previous value of the discharge

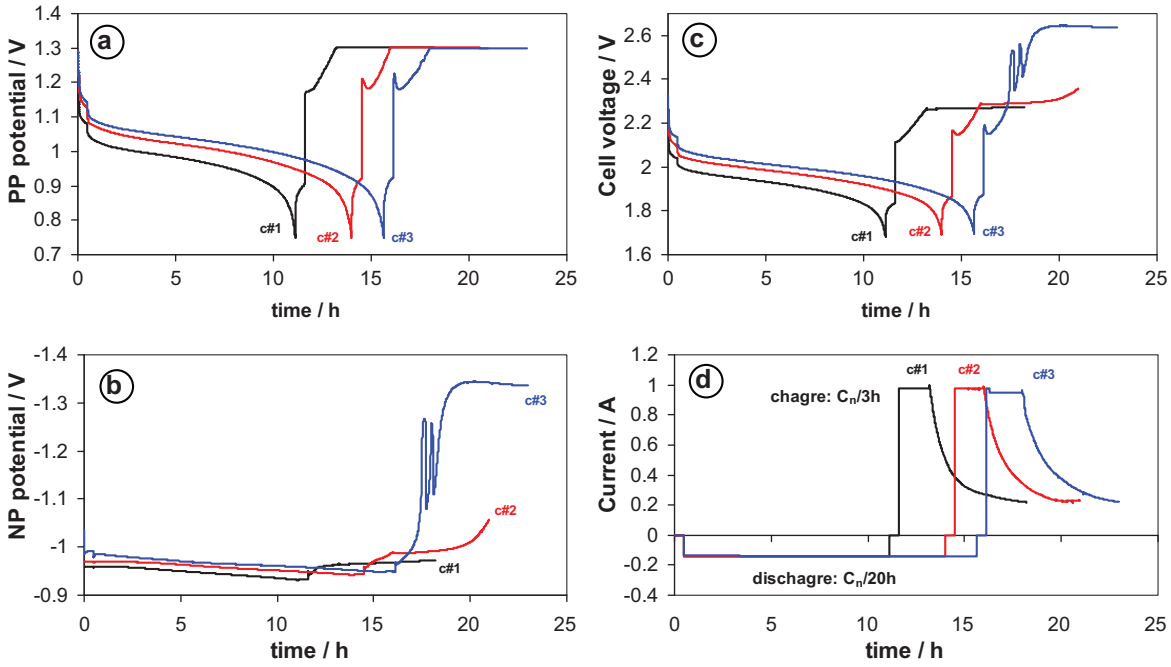

Fig. 12. Evolution of the positive (a) and the negative (b) half-cell potentials, the cell voltage (c) and the current (d) during the first three cycles of the VRLA cell testing.

capacity) in the range of 110–120%. Each 50 cycles the cell was subjected to several 20 h-rated discharge cycles in order to check the maximum utilisation of PAM. During these cycles the recharge regime was the same but with longer potentiostatic period.

The evolution of the cell parameters during cycle#105 and cycle#108 is presented in Fig. 14. The discharge curves of the positive plate potential (Fig. 14a) and the cell voltage are nearly identical. The total variation of the negative plate potential within the whole discharge is no more than 25–30 mV (Fig. 14c). The plateaux of the positive plate potential and the cell voltage in both discharge modes do not differ much form the data obtained in the beginning of the cycling. In C_n/5 h discharge mode the obtained capacity is 2.51 Ah corresponding to 44.3% utilisation of PAM. The application of smaller discharge current (C_n/20 h) allows reaching a capacity of 3.27 Ah and utilisation of PAM equal to 57.8%. Taking into account the honeycomb structure, these values are rather low. However two important details should be denoted. First the thickness of the positive plate is too big (~4 mm) which greatly impedes the discharge process in the middle of the honeycomb channels. The second detail is the insufficient quantity of the sulphuric acid due to the unfavourable ratio between the positive plate thickness and the AGM thickness (~2 mm). The latter can be proofed regarding the coefficient of sulphuric acid utilisation in 20 h-rated discharge mode—the value of 68.3% shows that the maximum capacity of the cell is limited rather by the electrolyte than by the lead dioxide in the positive plate.

The recharge transients of the positive plate potential for cycle#105 and cycle#108 are shown in Fig. 14d. It can be seen that the initial peak of the positive plate potential can be easy correlated with the depth of discharge—the peak is higher after the deeper C_n/20 h discharge. In potentiostatic mode the current decreases gradually until the positive plate is completely recharged and only oxygen evolution takes place with a current in the range of about 100 mA. The evolution of the negative plate potential during the charge (Fig. 14e) shows that the applied charge strategy using the positive plate potential instead of the cell voltage can be particularly useful for valve-regulated lead-acid cells and batteries. This strategy limits the rate of the oxygen evolution and thus the negative plate can be completely recharged due to the low rate of the oxygen recombination process. The oxygen recombination process works as a concurrent reaction of the lead sulphate reduction and the hydrogen evolution process. When the oxygen recombination takes place with considerable rate, it causes a depolarisation of the negative plate suppressing both the complete recharge and the hydrogen evolution [46]. The undesired consequences are two—a sulphation of the negative plate denoted as PCL-III (preliminary capacity loss) effect [46] or a thermal runaway [47], and both can be easy evaded using the reference electrode for charge regulation. A good evidence for this statement is the step-like increase of the negative plate polarisation in the end of the charge. The latter can be used even for end of charge criterion. Another advantage of this charge strategy is the total charge duration—if the increase of the negative plate polarisation is used as an end of charge indicator it can be seen that in cycle#108 the cell is recharged for 4 h and 6 min with charge factor of 107% until the inflection point, and the maximum of the negative plate polarisation is reached in 4 h 56 min at charge factor of 112%.

4.5. Performance of the prototype positive plate at the end of life

The cell was cycled with C_n/5 h discharge rate until cycle#181 when the discharge capacity was 0.93 Ah corresponding to 16.5% utilisation of PAM. Further, the cell was put to 10 cycles with C_n/20 h discharge rate for one last check of the maximum available utilisation of the active material. Fig. 15 presents the evolution of the cell parameters during cycle#180 (C_n/5 h discharge rate) and cycle#186 (C_n/20 h discharge rate). Despite the capacity loss, the discharge plateaux of the positive plate potential (Fig. 15a) and the cell voltage (Fig. 15b) are just slightly lower (~20–30 mV) in comparison with the data obtained during the cycles with maximum utilisation of PAM at the beginning of the cycling. At low-rate discharge regime the observed discharged capacity was 1.65 Ah corresponding to 29% utilisation of PAM (65 mAh g^{-1}). The evolution of the negative plates' potential during both cycles (Fig. 15c) is very close to the data presented in Fig. 14c, indicating no degradation of the negative active material.

The positive plate potential transients during the charge (Fig. 15d) are similar to the data obtained at the maximum capac-

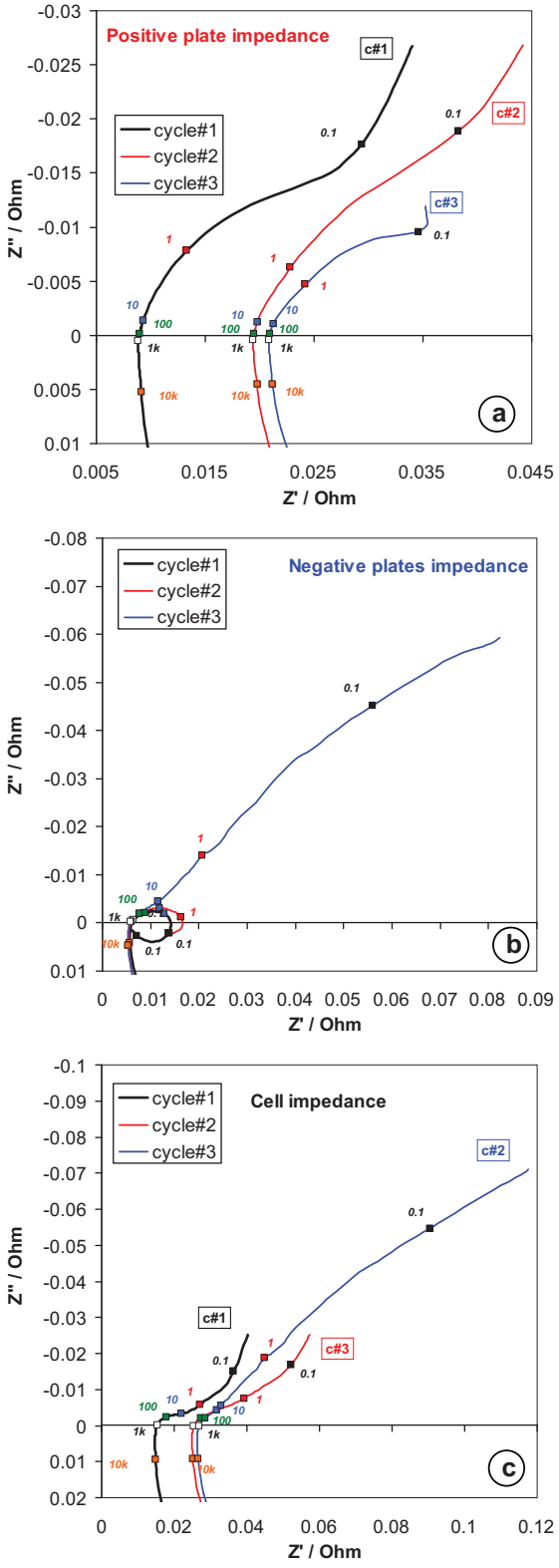

Fig. 13. Impedance spectra of the positive plate (a), negative plates (b) and the cell in the end of the charge for the first three cycles.

ity, however the peak in the in the beginning of the charge is higher and more narrow indicating increased resistance in the zone of the interface between the grid and the active material. It can be seen that after the application of C_n/20 h discharge cycles, the plateau of the positive plate potential at the constant charge current of C_n/1 h drops to about 1.36 V, which is only 30–40 mV higher than the corresponding value from Fig. 14d.

The recharge of the negative plates during cycle#186 (Fig. 15e) is similar to the above-discussed data. During the charge of the negative plates at cycle#180 the negative plates' polarisation increases fast in the initial galvanostatic stage due to the fact that in the previous discharge only a small portion of the negative active material is discharged. A second step-like increase of the negative plate polarisation is observed in the end of the complete cell recharge—it can be assumed that this second increase of the negative plate potential modulus denotes the "true" end of charge of the negative plates.

It should be noted here that the applied charge regime using the potential of the positive plate as a charge regulation parameters can be of great benefit for all types of VRLA batteries. This charge strategy works in totally opposite way during the ageing of the cells in comparison with the voltage-controlled recharge:

- it does not depend on the oxygen recombination rate and efficiency because this process takes place on the negative plate;
- it is slightly influenced by the AGM saturation and water loss. Moreover, while the decease of the AGM electrolyte saturation (due to the water loss along the ageing) causes increased end-of-charge current at fixed constant voltage charging and even thermal run away [48], the end of charge current in constant positive plate potential mode tends to the decrease with the drying-out of the AGM (or gel), because the oxygen overvoltage is higher in more concentrated sulphuric acid [49]. This self-regulation of the oxygen evolution rate with the advance of the ageing will decrease also the corrosion rate and thus the life of the VRLA battery will be prolonged additionally;
- a simple temperature control can be implemented using directly the data obtained about the temperature dependence of the oxygen evolution—according to Pavlov and Monahov using a temperature coefficient of 3.5–4 mV (°C)$^{-1}$ the rate of the of oxygen evolution can be kept constant over several decades Celsius [50].

4.6. Evolution of the positive plate impedance during the cycling

The impedance spectra of the positive plate and the cell were measured periodically in the end of the charge and in the end of the discharge after 30 min open circuit stay. The results for the case of completely charged positive plate are presented in Fig. 16. It can be seen that the most dramatic change in the impedance of the positive plate is the systematic shift of the real impedance towards higher values, obviously due to the advance of the grid corrosion processes. The cycling influences also to certain extent the general shape of the Nyquist plots. The spectra were fit with the equivalent circuit proposed by Pavlov and Petkova [51], shown in Fig. 16d as an inset. The results from the fitting are presented in Table 1. The magnitude and the evolution of the equivalent circuit parameters are similar to the ones obtained for flooded pasted positive plate with lead–antimony (2.8%) grid [49,52]. Thus it can be concluded that the ageing mechanism of the positive active mass does not differ substantially form the one typical for conventional positive plates. The values of the double layer capacitance follow roughly the discharge capacity:

- in the very beginning of the cycling the structure of PAM is still undeveloped corresponding to relatively low value of C_{dl};
- along the cycling, C_{dl} decreases, however a change in the discharge regime leading to better conversion of the lead dioxide into lead sulphate causes an increase of the C_{dl} value in the end of the subsequent charge.

The decrease of the C_{dl} value with the advance of the ageing can be correlated with the decrease of the BET surface area and the

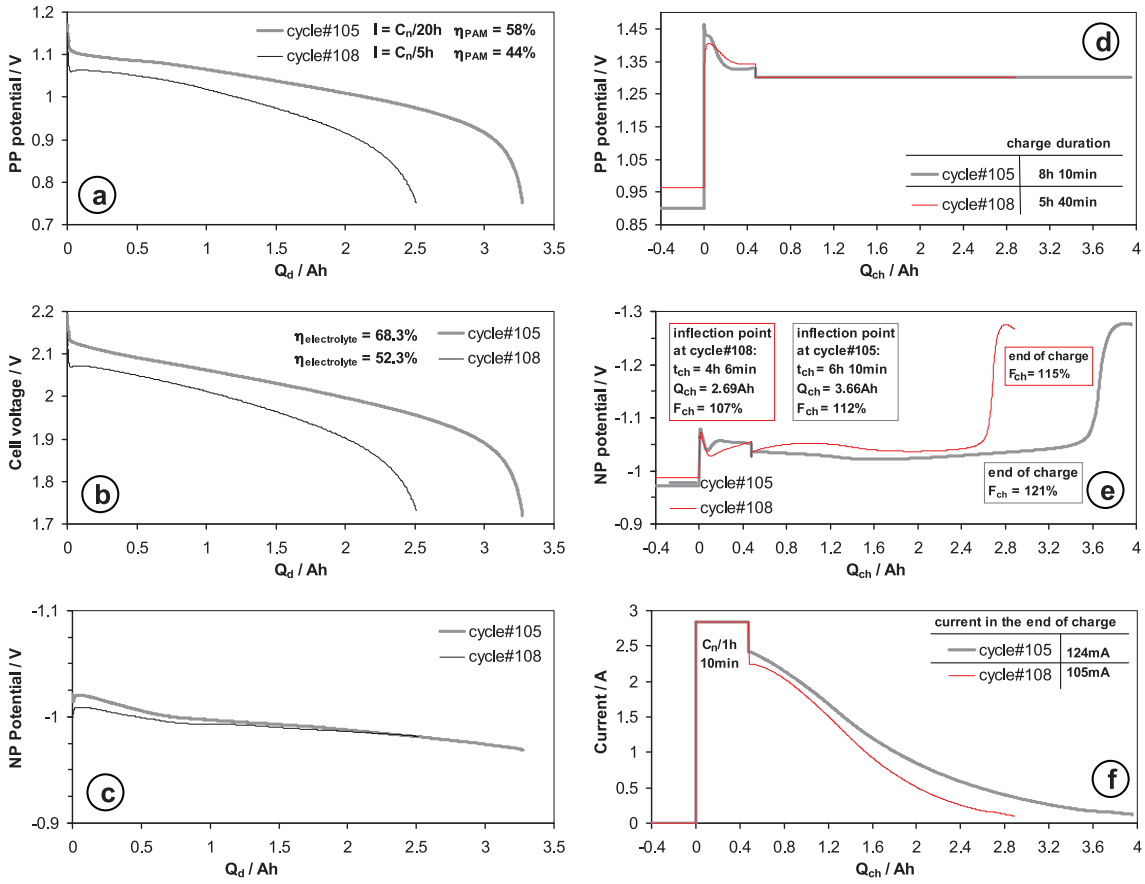

Fig. 14. Evolution of the VRLA cell parameters during cycle#105 and cycle#108.

increase of the particle size and crystallinity of PAM during deep cycling regimes observed by Dimitrov and Pavlov in [53].

Fig. 17 summarizes the evolution of the ohmic (or internal) resistance of the cell, the positive plate and the negative plates during the cycling at SoC = 100%. The increase of the cell ohmic resistance with the ageing corresponds perfectly to the evolution of the ohmic resistance of the positive plate. The ohmic resistance of the negative half-cell remains constant since the very first cycle. The increase of the positive plate internal resistance can be connected with the corrosion of the lead–tin coating and probably with a degradation of the carbon composite substrate. After cycle #159 the internal resistance of the cell becomes nearly constant suggesting that most of the lead–tin coating is corroded, i.e. converted into lead-dioxide. Despite this result the cell voltage plateau in the beginning of cycle#186 (Fig. 15d–f) at current $C_n/1$ h after the initial positive plate potential peak is about 2.48–2.50 V indicating still good electric performance of the carbon honeycomb grid.

4.7. Overview of the prototype cycling

The evolution of the normalized discharge capacity of the positive plate with the cycle number is presented in Fig. 18. For convenience the second *Y* axis gives also the percentage of the utilisation of PAM. It can be seen that the capacity remains high within about 160 cycles, after which it starts degrading fast. To a great extent this relatively short cycle life is due to the low quality of the paste—from one hand it was manually mixed and cured at room temperature and atmosphere conditions; from the other hand the high sulphate and water content corresponded to a density in the range of ~3.5 g cm^{-3} (precise measurement of the paste density was not possible). The cycle life curve of the $C_n/20$ h discharge capacity values resembles very much the base curve corresponding to the $C_n/5$ h discharge regime. Despite the low coefficients of the PAM utilisation (maxima of 47% at $C_n/5$ h and 60% at $C_n/20$ h discharge regimes), these results are very encouraging taking into account the big plate thickness (limiting the utilisation of PAM in the depth of the honeycomb cells) and the unfavourable AGM to PAM ratio corresponding to certain electrolyte insufficiency.

Fig. 18b presents the evolution of two charge parameters with the number of cycles:

- the charge factor representing the ratio between the injected Amp-hours during the charge and the previously obtained discharge capacity,

Table 1
Positive plate equivalent electric circuit parameters at state of charge equal to 100% obtained by the fitting of the corresponding impedance spectra with Z-View2® software.

Cycle number	Discharge capacity (Ah)	R_Ω (mΩ)	R_{ct} (mΩ)	C_{dl} (F)	Q_{diff} (F s$^{n\,diff-1}$)	n_{diff} (dimensionless)
2	1.90 (C/20 h)	19.2	0.5	10.24	37.06	0.45
10	2.18 (C/5 h)	23.6	0.6	21.19	38.54	0.73
51	2.67 (C/5 h)	37.8	0.4	18.37	72.39	0.75
102	2.35 (C/5 h)	40.4	0.5	14.50	103.6	0.77
159	2.73 (C/20 h)	56.4	0.6	17.00	175.0	0.67
182	1.12 (C/5 h)	56.0	1.0	5.513	142.7	0.62

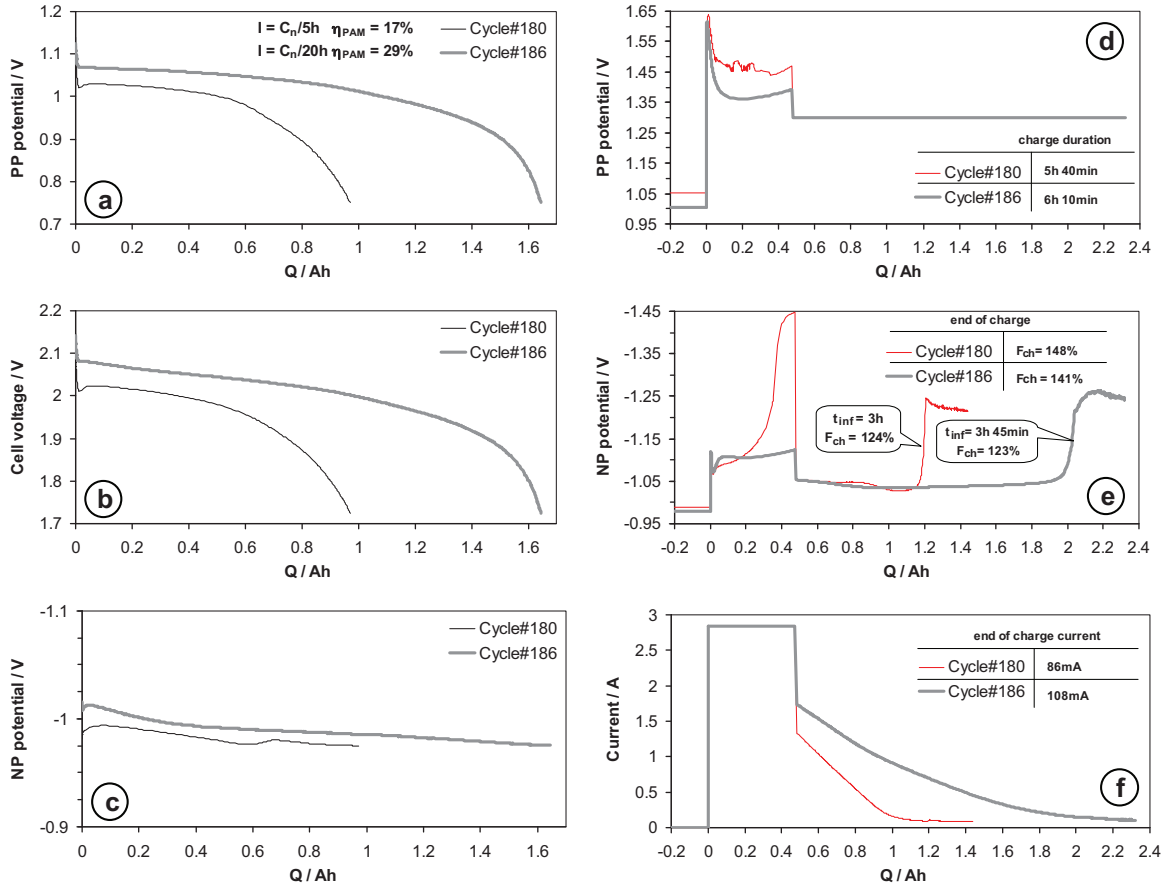

Fig. 15. Evolution of the VRLA cell parameters in the end of the cycle life.

- the end of charge current measured in the end of the potentiostatic stage represents roughly the rate of the oxygen evolution process on the positive plate.

The evolution of these two parameters suggests that the prototype grid is subjected to severe corrosion attack cased by the oxygen evolution process. Most of the time the charge factor is in the range of 130–140% (or more) and only within 20–30 cycles it is the range of 115–120%. The current at the end of the charge remains in the range of 100 mA ($\sim C_n/30$ h). Its value is slightly higher when the cell is discharged with smaller currents corresponding to higher DoD values. The cell voltage corresponding to the end of the charge current is in the range of 2.65 V in the beginning of the cycling and drops to 2.52–2.55 V after the first 40–50 cycles due to the increase of the oxygen cycle efficiency [54]. The application of such harsh overcharge strategy suggested that the capacity decay started after 80 cycles may be caused by drying-out of the AGM. That's why after cycle#132, 12 g of water were added in the cell on 2 g portions placing the cell in vacuum chamber for several minutes after each portion. In this way it was ensured the complete flooding of the active block. The evolution of the discharge capacity did not change after the addition of water, showing that even harsh, the applied charge strategy ensures good efficiency of the oxygen cycle and limited water loss.

After cycle #160 a faster capacity decline was observed in $C/5$ h discharge cycling mode. In the end of the cycling the cell was still able to deliver 58% of the nominal capacity in $C/20$ h discharged rated cycling regime. Generally the cycle life performance of the positive plate with carbon honeycomb grid is not much different from the typical positive plates with antimony-free grids [53].

Despite that the addition of water after cycle#131 did not influence the discharge capacity, it caused very interesting effects on the charge process. The first obvious effect is an increase of the charge factor right after the topping-up from ~115% to ~135% (Fig. 18b) as well as an increase of the current in the end of the potentiostatic charge stage. This can be related to the drop of the oxygen evolution overvoltage in more diluted sulphuric acid solutions [49]. A more detailed analysis of the influence of the water addition can be done comparing the current, voltage and potentials evolution during cycle #131 (just before the top-up) and cycle #133 (one cycle after the top-up) presented in Fig. 19. The comparison of the current evolution plotted in Fig. 19a shows very prominent increase of the charge acceptance after the water top-up, especially looking into the inset graph showing the evolution of the injected Amp-hours during the first two hours of the charge. In the end of this two-hour period for cycle #131 the charge factor is 88.5% while for cycle #133 its value is 112.6%, i.e. the positive plate is almost completely charged. The topping-up with water suppressed the operation of the oxygen cycle—since the transfer rate of the oxygen decreases through more saturated AGM separator, the cell voltage in the end of the charge increases due to the lower depolarisation oxygen cycle effect. Anyway, even before the water addition the complete recharge of the negative plates is well visible by the S-shaped increase of the negative half-cell polarisation from −1.05 to −1.25 V (vs. the reference electrode) demonstrating the robustness of the VRLAB charge strategy based on use of the integrated reference electrode.

The decrease of the electrolyte concentration causes a decrease of the cell electromotive force (emf). This effect can be seen well in Fig. 19b during the discharge and the subsequent open circuit

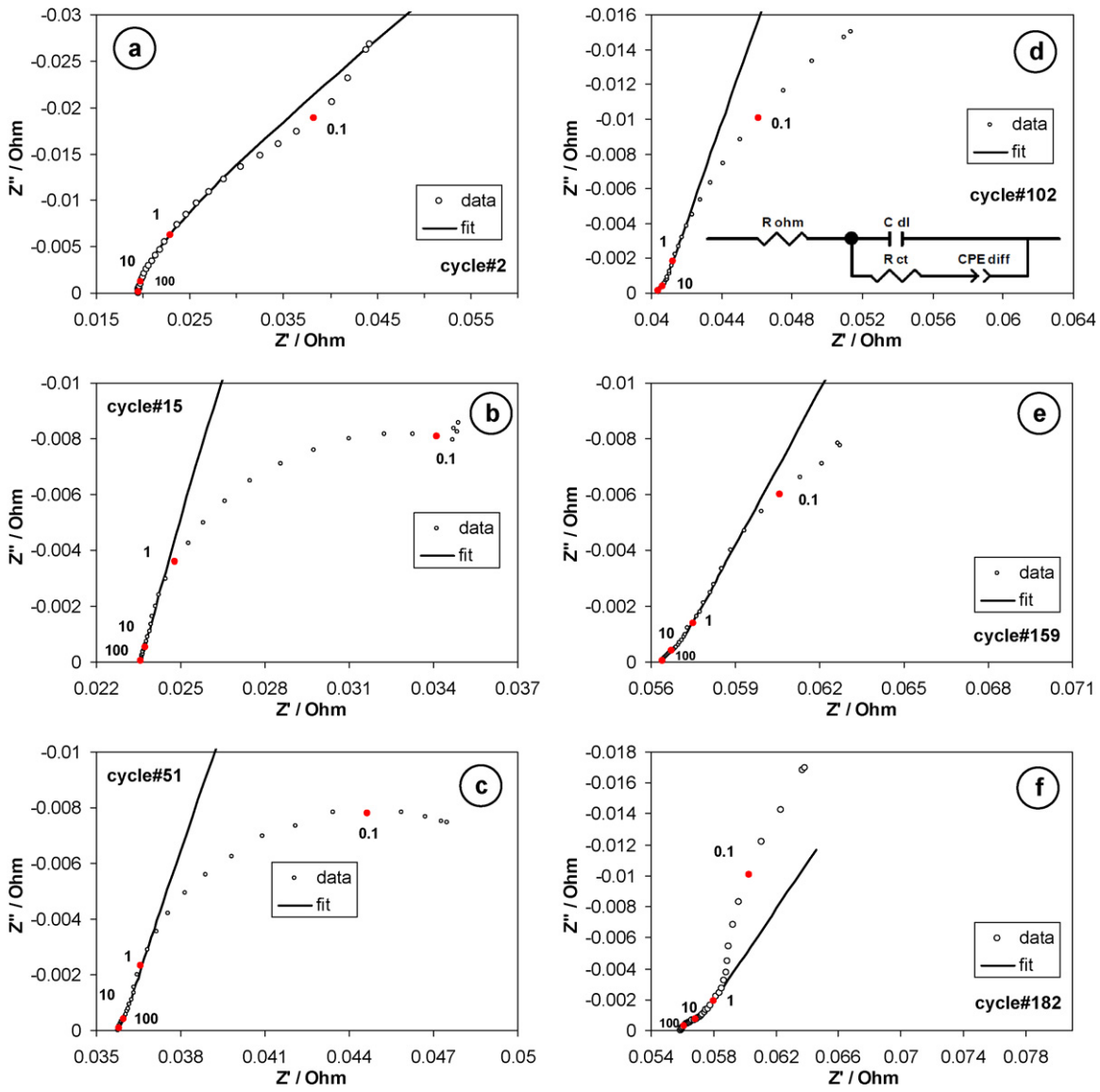

Fig. 16. Evolution of the positive plate impedance spectrum during the cycling at state of charge equal to 100%.

period. Surprisingly, both during the discharge and the open circuit periods the negative plate potential is much more influenced by the water addition. The comparison of the half-cell potentials and the cell voltage during the discharge before and after the water addition suggests that there is no change of the ohmic resistance components within the cell.

The increase of the charge acceptance after the addition of water is also very obvious comparing the positive plate potential evolution in the beginning of the charge. Here, the positive plate potential peak associated with the resistance of the interface between the PAM and the grid is reduced with about 150 mV. Taking into account the constant current of 2.83 A during this potential peak, the reduction of the polarisation resistance after the water addition is in the range of 53 mΩ, i.e. a value comparable with the cell internal resistance. However, from the other hand if the positive plate potential plateau after the peak is considered as a base line instead of the open circuit potential, the resulting relative peak height is nearly the same. Thus it can be concluded that the effect of the water addition is focused in the volume of PAM rather than at the interface PAM/grid.

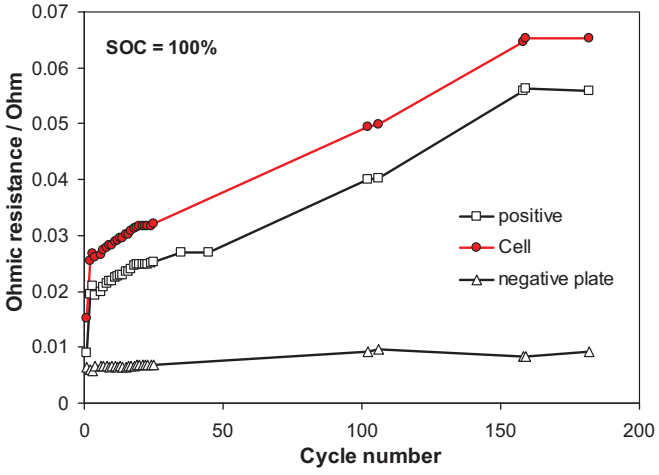

Fig. 17. Evolution of the ohmic (internal) resistance of the cell, positive plate and negative half-cell during the cycling at state of charge equal to 100%.

4.8. Post mortem analysis of the cell

The cell was subjected to tear down analysis after 191 cycles. Both negative plates were in excellent condition with homogeneous grey colour. The positive active material was with homogenous dark brown colour. The patterns of the honeycomb cells are also visible.

The attempt to separate the positive plate from the second negative plate resulted in easy breaking of the plate into several pieces indicating that the carbon composite lost part of its mechanical strength. Despite that there was no shedding of PAM. The active material was very soft, with a paste-like texture. Great part of it was washed away by the water in the subsequent electrolyte removal process. This softening of the active material can be pointed out as the main cause for the capacity fade.

In order to investigate further the plate and grid degradation, washed and dried fragments of the positive plate together with the active material were embedded in epoxy resin and prepared for microscopy observations. It was found that lead–tin coating in the zone of the frame was not completely corroded, while no metallic lead was visible in the honeycomb part of the grid. Fig. 20a shows stereo-microscope image of few honeycomb cells filled with PAM located between two thicker plain-parallel sheets. It can be seen that the thicker plain-parallel sheets contain cracks and fractures typically in direction perpendicular to the sheet. The optical micrograph from Fig. 20b gives a closer look to the zone of the node point between the corrugated and the plain sheet. Here one can see that the cracks also differ in size. In the present moment it is hard to conclude if these cracks have purely mechanical origins due to the volume expansion of PAM during the discharge (so-called breathing) or there is also a corrosion contribution due to the oxygen evolution process. The answer to this question will be given in a next publication which will be focused on the performance of negative plates with carbon honeycomb grids. In this case, the issues with the corrosion will be eliminated completely while the

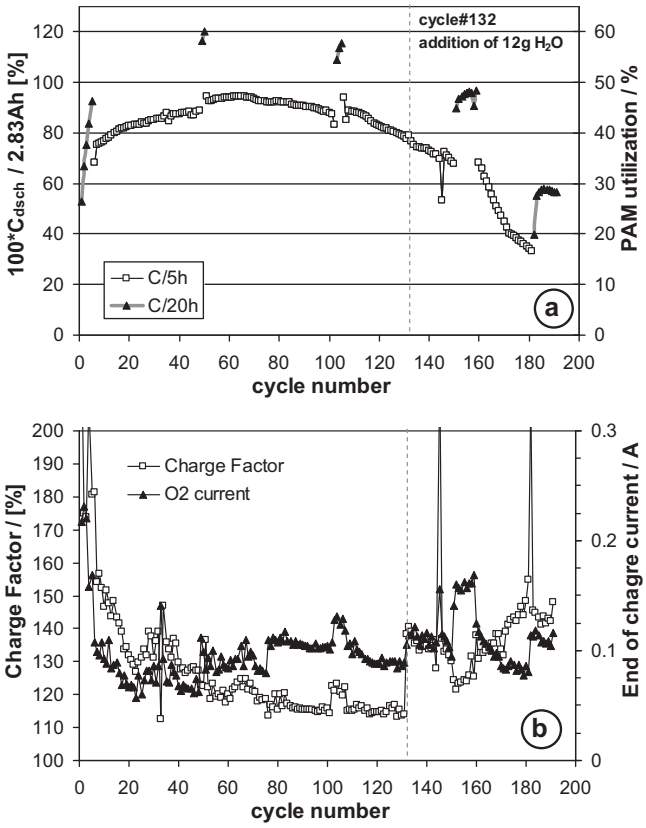

Fig. 18. Evolution of the normalized VRLA cell capacity, the utilisation PAM (a), the charge factor and current in the end of the charge (c) with the number of charge/discharge cycles.

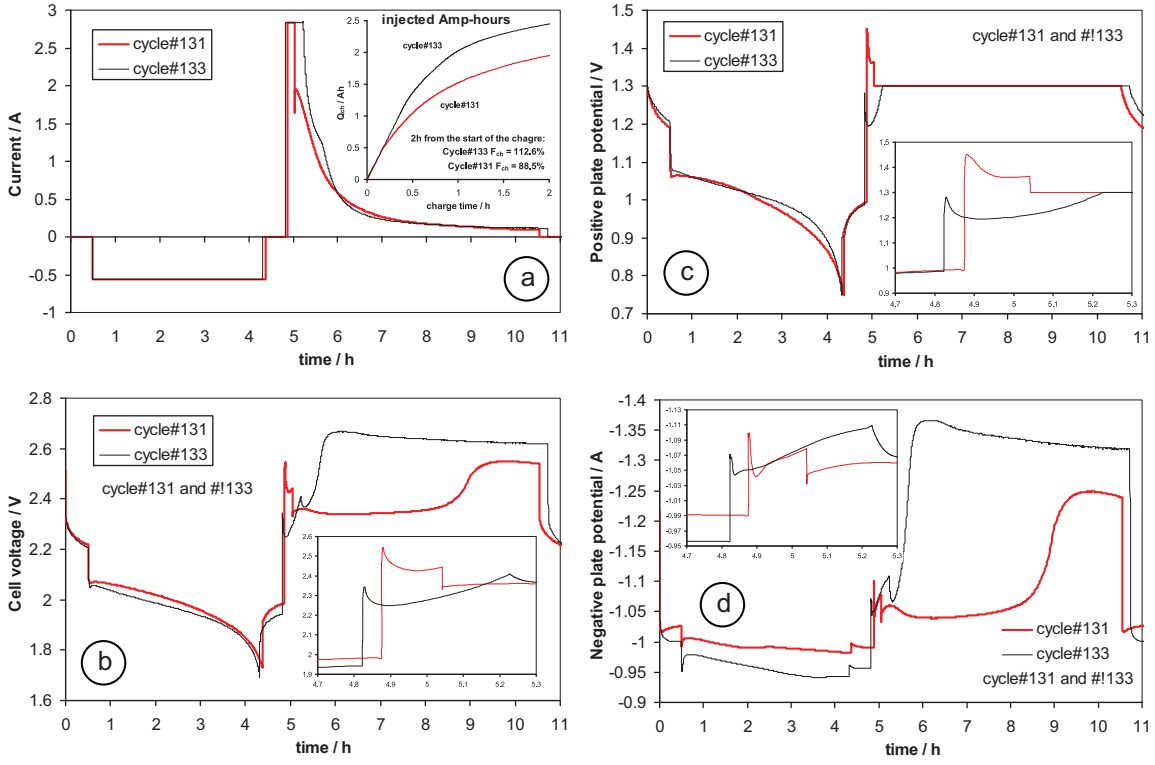

Fig. 19. Evolution of the VRLA cell parameters before (cycle#131) and after (cycle#133) the top-up with water.

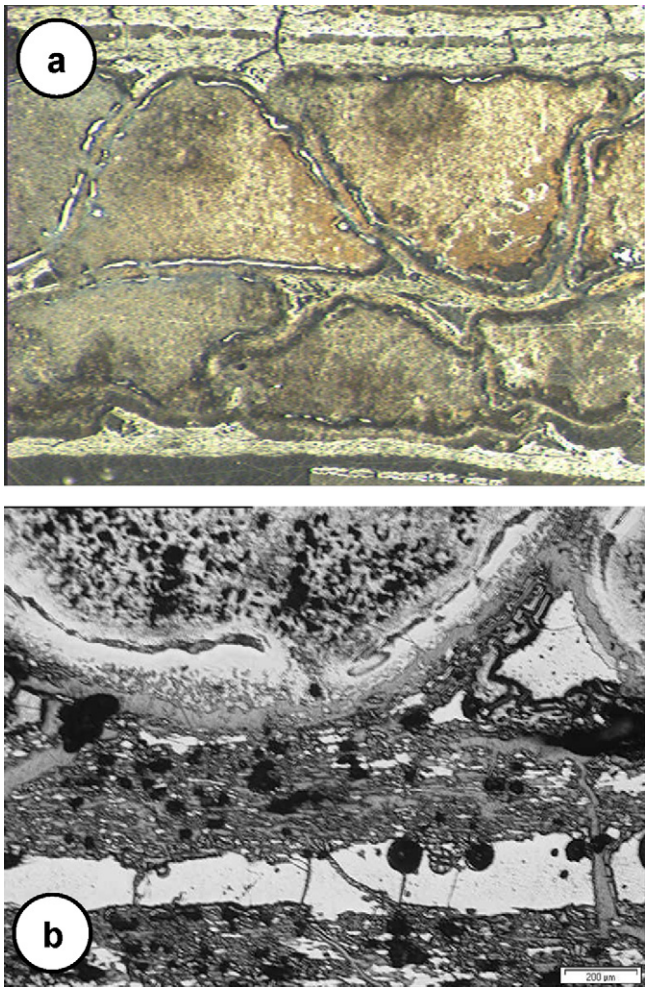

Fig. 20. Stereo-microscope image (a) of few honeycomb cells filled with PAM located between two thicker plain-parallel sheets and optical micrograph (b) of the node zone between a corrugated and plain-parallel grid fragment.

mechanical stress excreted by the volume expansion of NAM will be much greater.

The selected appearance of cracks in the ticker plain-parallel section of the carbon honeycomb is a clear indication that the quality and the structure of the honeycomb core is a critical parameter. It can be expected that hexagonal industrial grade honeycomb cores which are properly impregnated with resins could deliver longer cycle life. The hexagonal core with slightly higher or same cell size can result into a structure with smaller surface, i.e. the quantity of the electrodeposited lead–tin alloy will be less keeping the same grid mesh size, resulting in better PAM to grid weight ratio especially using 4BS pastes with density in the range 4.1–4.15 g cm^{-3}.

5. Conclusions and perspectives

The carbon honeycomb grid concept was demonstrated as an advanced lead-acid battery positive plate current collector. The technology features numerous advantages:

- Low cost starting materials like cellulose paper honeycombs impregnated with thermosetting resins (including resins from renewable bio-sources).
- Use of simple and low cost processes like resin moulding and band saw cutting during the manufacturing of the green composite grids
- Fast carbonisation process in the range 200–1000 °C resulting in low energy consumption (in terms of heating and nitrogen atmosphere delivery) and high production rate.
- Lead–tin or pure lead electroplating resulting in coatings with excellent corrosion resistance.
- Use of conventional pastes, curing and formation.
- Optimal grid architecture resulting in very low gamma coefficients (∼0.15 g cm^{-2}) ensuring good cycle life.
- Excellent compatibility with the AGM VRLA battery technology.

The post mortem analysis of the first prototype cell showed that the softening of PAM is the main reason for the capacity decay. The corrosion of the grid was very severe due to the applied charge regime

- the lead–tin coating in the zone of the honeycomb core was completely corroded;
- the structure of the carbon/carbon composite was damaged resulting in loss of mechanical strength due to the appearance of cracks preferentially in the thicker plane-parallel zone of the carbonised honeycomb.

Despite the corrosion processes, the electric performance of the positive plate remained acceptable—the increase of the positive plate impedance was not high enough to cause an appearance of substantial voltage drop during the 5 h-rated discharge in the end of the cycling. It is expected that the use of industrial grade of honeycomb core materials with hexagonal cell geometry and high quality of the processes of bonding and impregnation will improve considerably the performance of the grids.

An innovative VRLA battery charge strategy was demonstrated. It is based on the regulation of the positive plate potential instead of the VRLA cell or battery voltage using an integrated reference electrode. Such a strategy allows the reduction of the charge time without any sacrifice of the battery safety in terms of thermal runaway or drying out. The charge algorithm can be easy optimised towards low positive grid corrosion rates decreasing the value of the positive plate potential during the potentiostatic charge stage. In this way, the water loss will be decreased too.

Two important questions considering the carbon honeycomb grid technology remained open

- What is the maximum acceptable charge/discharge rate of grids without lead or lead–tin coating?
- What is the impact of the active materials breathing on the structural integrity of the carbon/carbon composite material?

The answers of both questions will be amongst the main objectives of the next publication in this series focused on the application of the carbon honeycomb grids for lead-acid battery negative plates.

Acknowledgments

This work was financially supported by the E-ON International Research Initiative as part of the project “BEST – Benefits of the Storage Systems for Grid-Connected and Advanced Vehicle Applications”.

The phenol-formaldehyde resins used in the development of the carbon honeycomb grids were kindly supplied by HEXION Specialty Chemicals, Inc., Louisville, KY, USA, presently Momentive Specialty Chemicals Inc. AK would like to thank Mr Bill Handel from HEXION (presently Momentive) for the useful discussions about the choice of the resin types to be used in this work. The delivery of casings

for VRLA cells by First National Battery (Republic of South Africa) is gratefully acknowledged.

The authors would like to thank Mr. David Brun-Buisson (CEA-INES) and Mr. Frank Haladjian (CEA-INES) for the technical support in the microscopy observations and in the mechanical workshop of INES.

References

[1] A.J. Salkind, A.G. Cannone, F.A. Trumbure, in: D. Linden, T.B. Reddy (Eds.), Lead-acid Batteries, 3rd ed., McGraw-Hill, New York, 2002, p. 23.17 (Chapter 23).
[2] I. Petersson, E. Ahlberg, J. Power Sources 91 (2000) 143–149.
[3] A. Czerwiński, M. Żelazowska, J. Electroanal. Chem. 410 (1996) 55–60.
[4] A. Czerwiński, M. Żelazowska, J. Power Sources 64 (1997) 29–34.
[5] E. Gyenge, J. Jung, S. Splinter, A. Snaper, J. Appl. Electrochem. 32 (2002) 287–295.
[6] E Gyenge, J. Jung, B. Mahato, J. Power Sources 113 (2003) 388–395.
[7] A. Czerwiński, S. Obrębowskia, J. Kotowski, Z. Rogulski, J.M. Skowrońskic, P. Krawczyk, T. Rozmanowski, M. Bajsert, M. Przystałowski, M. Buczkowska-Biniecka, E. Jankowska, M. Baraniak, J. Power Sources 195 (2010) 7524–7529.
[8] A. Czerwiński, S. Obrębowski, J. Kotowski, Z. Rogulski, J. Skowroński, M. Bajsert, M. Przystałowski, M. Buczkowska-Biniecka, E. Jankowska, M. Baraniak, J. Rotnicki, M. Kopczyk, J. Power Sources 195 (2010) 7530–7534.
[9] K.C. Kelley, J.J. Votoupal, Battery including carbon foam current collectors, patent number US 6,979,513.
[10] K.C. Kelley, C.F. Ostermeier, M.J. Maroon, Composite material and current collector for battery, patent number US 7,033,703.
[11] N. Brazis, K.C. Kelley, M.J. Maroon, B. Monahov, Composite carbon foam, patent application number WO 2008/020052 A1.
[12] B. Monahov, K. Kelley, M. Alkhateeb, Organic additives for improving performance of lead-acid battery, patent applications WO 2010/008966 A1.
[13] Y. Chen, B.-Z. Chen, X.-C. Shi, H. Xu, Y.-J. Hu, Y. Yuan, N.-B. Shen, Carbon 45 (2007) 2132–2134.
[14] Y. Chen, B.-Z. Chen, X.-C. Shi, H. Xu, W. Shang, Y. Yuan, L.-P. Xiao, Electrochim. Acta 53 (2008) 2245–2249.
[15] Y. Chen, B.-Z. Chen, L.-W. Ma, Y. Yuan, Electrochem. Commun. 10 (2008) 1064–1066.
[16] Y. Chen, B.-Z. Chen, L.-W. Ma, Y. Yuan, J. Appl. Electrochem. 38 (2008) 1409–1413.
[17] L.-W. Ma, B.-Z. Chen, Y. Chen, Y. Yuan, J. Appl. Electrochem. 39 (2009) 1609–1615.
[18] Y.-I. Jang, N.J. Dudney, T.N. Tiegs, J.W. Klett, J. Power Sources 161 (2006) 1392–1399.
[19] J.W. Klett, Process for making carbon foam, patent number US 6,033,506.
[20] D. Pavlov, J. Power Sources 53 (1995) 9.
[21] A. Kellomaki, J. Rautavuori, J. Mater. Sci. 15 (1980) 1317.
[22] M. Noel, P.N. Ananthraman, Surf. Coatings Technol. 28 (1986) 161–179.
[23] G.K. Kiema, S. Ssenyange, M.T. McDermott, J. Electrochem. Soc. 151 (2004) C142–C148.
[24] T. Rapecki, A.M. Nowicka, M. Donten, F. Scholz, Z. Stojek, Electrochem. Commun. 12 (2010) 1531–1534.
[25] A. Kirchev, N. Kircheva, Acid-lead battery electrode comprising a network of pores passing there through, and production method, Patent publication WO2010115705 (A1), 14 October 2010.
[26] T.N. Bitzer, Honeycomb Technology: Materials, Design, Manufacturing, Applications and Testing, Chapman and Hall, London, 1997, October.
[27] C.R. Schmitt, Carbon 7 (1969) 635–3642.
[28] J. Alcañiz-Monge, C. Blanco, A. Linares-Solano, R. Brydson, B. Rand, Carbon 40 (2002) 541–550.
[29] H. Bode, Lead-acid Batteries, John Wiley & Sons, New York, 1977, pp. 156–159.
[30] P. Faber, in: D.H. Collins (Ed.), Power Sources, vol. 4, Oriel Press, Newcastel upon Tyne, 1974, pp. 525–538.
[31] International standard ISO 2144:1997 Paper, board and pulps – determination of residue (ash) on ignition at 900 °C.
[32] J. Rautavuori, P. Törmälä, J. Mater. Sci. 14 (1979) 2020–20222.
[33] G.M. Jenkins, K. Kawamura, Polymeric Carbons–carbon Fibre, Glass and Char, Chapter 2: Pyrolysis of Polymers, Cambridge University Press, Cambridge, 1976, pp. 11–35.
[34] H. Maleki, L.R. Holland, G.M. Jenkins, R.L. Zimmerman, Carbon 35 (1997) 227–234.
[35] SIGRADUR® K physical properties datasheet, HTW website, www.htw-gmbh.de/technology.
[36] L.G. Zaltsamn, S.M. Tchernaya, Sputnik galvanika (Elelctroplater's satellite), 3rd ed., Tehnika, Kiev, 1989, pp. 76, 79 (in Russian).
[37] V.I. Ignatiev, Galvanitcheskie pokritia v mashinosroenii (Galvanic coatings in the machine-building industry) vol. 1 in: M.A. Shluger (ed.), Glava 11 Olovianirovanie i svintsevanie (Chapter 11 Tin and lead plating), Mashinostroenie, Moskva, 1985, p. 210 (in Russian).
[38] V.A. Ilin, Luzhenie i svintsevanie (Tin and Lead Plating), Mashinostroenie, Leningrad, 1971, p. 29 (in Russian).
[39] A.M. Yampolskii, V.A. Ilin, Kratkii spravochnik galvanotehnika (Short Electroplater's Handbook), 3rd ed., Mashinostroenie, Leningrad, 1981, p. 121 (in Russian).
[40] M.A. Belnenkii, A.F. Ivanov, Elektroosazhdenie metalicheskih pokritii – spravotchnik (Handbook of Metal Coatings Electrodeposition), Moskva Metallurgia, 1985, pp. 89, 173 (in Russian).
[41] P. Ruetschi, J. Power Sources 116 (2003) 53–60.
[42] P. Ruetschi, J. Power Sources 113 (2003) 363–370.
[43] A.N. Campbell, R.M. Screaton, T.P. Schaefer, C.M. Hovey, Can. J. Chem. 33 (1955), 551–526.
[44] D. Pavlov, G. Petkova, M. Dimitrov, M. Shiomi, M. Tsubota, J. Power Sources 87 (2000) 39–56.
[45] D. Pavlov, G. Petkova, J. Electrochem. Soc. 149 (2002) A644–A653.
[46] R.F. Nelson, E.D. Sexton, J.B. Olson, M. Keyser, A. Pesaran, J. Power Sources 88 (2000) 44–52.
[47] D. Pavlov, Thermal phenomena during operation of the oxygen cycle in VRLAB and processes that cause them, J. Power Sources 158 (2006) 964.
[48] Y. Guo, S. Tang, G. Meng, S. Yang, J. Power Sources 191 (2009) 127–133.
[49] A. Kirchev, A. Delaille, F. Karoui, M. Perrin, E. Lemaire, F. Mattera, J. Power Sources 179 (2008) 808–818.
[50] D. Pavlov, B. Monahov, J. Electrochem. Soc. 145 (1998) 70–77.
[51] D. Pavlov, G. Petkova, J. Electrochem. Soc. 149 (2002) A654–A661.
[52] A. Kirchev, A. Delaille, M. Perrin, E. Lemaire, F. Mattera, J. Power Sources 170 (2007) 495–512.
[53] M. Dimitrov, D. Pavlov, J. Power Sources 93 (2001) 234.
[54] A. Kirchev, D. Pavlov, J. Power Sources 162 (2006) 864–869.